Article

Tuning binding strength between single metal atoms and supports enhances electrochemical CO_2 methanation

Linbo Li[1,2,7], Xin Lei[1,3,7], Zhilong Zheng[1,4], Yingjun Dong[1], Haohui Chen[1], Jun Chen [5], Yi Zhong[1], Yongping Zheng [1], Yongbing Tang [1,2] ✉, Xiaolong Zhang [1,2] ✉ & Hui-Ming Cheng [1,2,6] ✉

Single-atom catalysts (SACs) with tunable site density and activity are promising for catalytic processes. However, the relationship between interacting sites and the catalytic mechanism, as well as the effect of the support on this relationship, remains incompletely understood. Here we report a support geometry engineering strategy to control the inter-site distance (d_{site}) of Cu–N–C (CuNC) SACs via strong interactions between CuNC and a secondary support (ss). This process allows tuning of the binding strength (that is Cu–N bond length) between individual Cu atoms and the N-doped primary supports, concomitantly suppressing defect formation and Cu atom detachment in the CuNC framework. The continuous optimization of the electronic and coordination structure of individual active Cu sites, achieved by reducing the d_{site} to approximately 0.7 nm, enhances their inherent CO_2-to-methane selectivity and activity. As a result, the ss-engineered CuNC with a moderate d_{site} of 0.68 nm exhibits enhanced methane selectivity of 70% and a partial current density of 303.9 mA cm^{-2}, over 1.5 times higher than that of unmodified CuNC.

The electrochemical CO_2 reduction reaction (CO_2RR) powered by renewable energy is a promising strategy to achieve efficient and sustainable production of green fuels and chemical feedstocks[1–4]. Among CO_2RR electrocatalysts, copper (Cu)-based catalysts can efficiently catalyse CO_2RR for the production of hydrocarbons and oxygenates[5–9]. Of these products (such as methanol, methane, ethylene, ethanol, etc.), methane (CH_4) stands out as a fuel with high combustion efficiency and the highest energy density (~56 kJ/g), and is widely used in the energy and chemical industries[10]. Green energy-powered electrochemical CO_2 methanation (ECM) eliminates the high emissions associated with fossil CH_4 extraction and offers a promising opportunity to close the anthropogenic carbon cycle.

However, bulk Cu exhibits limited CO_2RR selectivity toward CH_4 under ambient conditions[11,12]. As the dimensions of Cu catalysts gradually decrease to the atomic scale, their selectivity for CH_4 increases correspondingly, due to the high energy barrier for C–C dimerization and favourable protonation of the key *CHO intermediate at Cu-single-atom (Cu SA) sites[13–17]. Results from previous theoretical and experimental studies show that the modification of the coordination and electronic structures of Cu SA sites is critical for highly efficient and selective CH_4 production over Cu SA catalysts (Cu SACs, Supplementary Table 1)[15–21]. Inspired by the role of Cu–C bonds in altering organic reaction pathways in organometallic coordination chemistry, Wang et al. constructed Cu–C bonds to stabilize Cu SA sites on graphdiyne

[1]Shenzhen Key Laboratory of Energy Materials for Carbon Neutrality, Shenzhen Institute of Advanced Technology, Chinese Academy of Sciences, Shenzhen, China. [2]Faculty of Materials Science and Energy Engineering, Shenzhen University of Advanced Technology, Shenzhen, China. [3]Shenzhen College of Advanced Technology, University of Chinese Academy of Sciences, Shenzhen, China. [4]School of Physics, Huazhong University of Science and Technology, Wuhan, China. [5]Intelligent Polymer Research Institute, Innovation Campus, University of Wollongong, Squires Way, North Wollongong, NSW, Australia. [6]Shenyang National Laboratory for Materials Science, Institute of Metal Research, Chinese Academy of Sciences, Shenyang, China. [7]These authors contributed equally: Linbo Li, Xin Lei. ✉e-mail: tangyb@siat.ac.cn; xl.zhang@siat.ac.cn; hm.cheng@siat.ac.cn

via a unique electronic regulation effect between graphdiyne and Cu. This strategy accelerates charge transfer, changes the electronic structure of Cu atoms, and promotes the formation of *OCHO intermediates and the reaction pathway to CH_4[18]. The introduction of a second non-metal element (O/B/N) into the first coordination shell of Cu SA changes the oxidation state and optimizes the adsorption of *CO and *CHO intermediates for highly selective CH_4 conversion[19,20]. Despite significant advances in ECM, the correlation of the density and proximity effect of active Cu sites in supported Cu SACs with their activity and selectivity toward CH_4 has rarely been investigated[22–25]. Furthermore, a deep atomic-level understanding of the support effect on this correlation is required.

Recently, a proof-of-concept study of Fe–N_4 SACs for oxygen reduction reaction (ORR) unveiled the connection between the origin of enhanced ORR activity and the kinetic property of isolated active sites as well as the proximity effect of neighbouring metal atoms using a descriptor of inter-site distance (d_{site})[26]. However, the support effect on the d_{site} effect and the resulting reactivity should also be taken into account. Here, we report a support geometry engineering strategy to control the d_{site} effect, as well as the electronic and coordination structure of CuN_4 SAs anchored on a N-doped carbons (CuNC), where N-doped carbons (NC) serves as the primary support. This is achieved via conformal coating of polydopamine on the secondary support (graphite flakes, also denoted as ss), which plays a crucial role in shaping the geometry and curvature of CuNC. This process facilitates the continuous and uniform anchoring of homogeneous CuN_4 SAs over a broad range of site density. Strong interactions between CuNC and ss efficiently steer the binding strength (that is Cu–N bond length) between individual Cu atoms and their primary supports, thereby mitigating sintering and further tuning d_{site} in ss-engineered CuNC (ssCuNC). Such interactions also enable charge transfer from the CuNC to the ss, leading to an elevated oxidation state of the CuN_4 SAs in the ssCuNC. Theoretical modelling suggests that reducing the d_{site} of CuN_4 SAs to ~0.7 nm enhances their structural stress without changing the ECM reaction pathway. This enhancement shortens the Cu–N bond length and induces a positive shift in the $3d_{x^2-y^2}$ orbitals of Cu, thus improving the adsorption capacity and catalytic activity of individual active Cu sites for CH_4 generation. Computational results also indicate that a low d_{site} value not only stabilizes *CO adsorption due to the elevated $d_{x^2-y^2}$ orbital level but also favours protonation of *OCH_3 to form CH_4. This is consistent with in situ spectroscopic results showing that selective electrosynthesis of CH_4 occurs at the expense of *CO, which shows a strong adsorption signal on ssCuNC. As a result of this strategy, ssCuNC with a moderate d_{site} of 0.68 nm and enhanced intrinsic site reactivity exhibits increased CO_2-to-CH_4 selectivity of 70% and a partial current density of 303.9 mA cm^{-2}, which is at least 1.5 times higher than that of all other CuNC materials.

Results

Identification of the role of support geometry engineering in the synthesis of Cu SACs with different d_{site} values

The synthesis principle related with support geometry engineering was first studied. Polydopamine (PDA), derived from the self-polymerization and oxidation of dopamine, was used as a metal carrier to chelate Cu^{2+} ions via its rich oxygen-containing functional groups, producing uniformly dispersed discrete Cu-chelated PDA nanoparticles (PNP–Cu) under alkaline conditions (Fig. 1a, b and Supplementary Fig. S1)[27,28]. A series of PNP–Cu precursors were synthesized with designated $CuSO_4$ concentrations, such as 0.29 mg ml^{-1}, 0.57 mg ml^{-1}, 0.71 mg ml^{-1}, and 1.14 mg ml^{-1} (Supplementary Fig. S1 and Methods). To verify the role of support geometry in fabricating Cu SACs with different d_{site} values, chemically inert planar graphite flakes were introduced as a secondary support (ss) to engineer the geometry of PDA (Supplementary Fig. S2). Strong covalent and noncovalent interactions between PDA and the substrate enable the formation of a

PDA film conformally coated on ss[29]. Oxidation of dopamine by Cu^{2+} produces integrated, continuous Cu-chelated PDA nanoparticles and films conformally coated on ss (ss–PNF–Cu; Supplementary Fig. S3). For these amorphous PNP–Cu and ss–PNF–Cu precursors, no metallic Cu or Cu-related carbides/nitrides were identified in powder X-ray diffraction (XRD) pattens, suggesting that PDA was complexed with Cu ions via its catecholate groups rather than reducing Cu^{2+} to metallic Cu (Supplementary Fig. S4).

As the $CuSO_4$ concentration increased from 0.29 to 1.14 mg ml^{-1}, the obtained PNP–Cu precursors exhibited comparable PNP size (0.12–0.15 µm), while the weight of PNP–Cu nanoparticles increased significantly from 0.042 to 0.28 g (Supplementary Figs. S5a–d, Fig. S6a, c and Supplementary Table 2). This finding implies that increasing the Cu^{2+} concentration promotes the generation of more PNP–Cu nanoparticles with similar sizes, rather than substantially increasing the size of individual PNP–Cu nanoparticles. In contrast, the average PNP size of as-prepared ss–PNF–Cu precursors increased linearly from 0.07 µm to a peak of 0.15 µm, and the weight of ss–PNF–Cu precursors increased significantly from 0.2 to 0.45 g (Supplementary Figs. S5e–h and S6b, d). The difference in average PNP size between PNP–Cu and ss–PNF–Cu precursors is ascribed to the competitive growth of PNF in ss–PNF–Cu precursors. This is supported by the observation that the coverage area of PNF–Cu coated on ss increased with increasing $CuSO_4$ concentration (Supplementary Fig. S3). These geometric features of PNP–Cu and ss–PNF–Cu are depicted in Fig. 1a, b. These results also indicate that redox-active Cu^{2+} contributes to the self-polymerization and oxidation of dopamine but has only a slight effect on the kinetics of dopamine polymerization under basic conditions[28,30,31]. In contrast to the similar geometry of spherical PNP–Cu precursors, the varied geometry combinations of spherical PNP–Cu and planar Cu-chelated PDA films in ss–PNF–Cu precursors provide a platform for modulating site density diversity, which is enabled by the support engineering.

The as-prepared PNP–Cu precursors were further uniformly ground with dicyandiamide powder (DCD, N source). The ground mixture was then pyrolyzed to generate atomic Cu sites anchored to N-doped carbon (CuNC; Fig. 1a, c; see Methods). Using ss–PNF–Cu precursors and the same synthesis procedure as for CuNC preparation, the ss-engineered CuNC (ssCuNC) catalysts were generated (Fig. 1b, d). According to the $CuSO_4$ concentration used, the resulting CuNC catalysts were designated as CuNC40, CuNC80, CuNC100, and CuNC160 (Supplementary Fig. S7). Correspondingly, the resulting ssCuNC catalysts were designated as ssCuNC40, ssCuNC80, ssCuNC100, and ssCuNC160 (Supplementary Fig. S8). No metallic Cu species were detected in any of the CuNC and ssCuNC catalysts (Supplementary Fig. S9).

Elemental analysis of the precursors was carried out using inductively coupled plasma mass spectrometry (ICP-MS) and X-ray photoelectron spectroscopy (XPS). Supplementary Fig. S10 shows that the Cu content in PNP–Cu and ss–PNF–Cu precursors increases almost linearly with increasing Cu^{2+} concentration, demonstrating the robust Cu-complexing capability of PDA over the entire range of Cu^{2+} concentration range used (Supplementary Table 2). This ensures that Cu^{2+} ions are homogeneously distributed throughout the PDA-based precursors within the specified concentration range. The correlation between Cu content in PDA-based precursors and in the corresponding Cu SACs was also studied. When the applied Cu^{2+} concentration is less than 0.71 mg ml^{-1}, a positive linear correlation exists between Cu loading in both CuNC and ssCuNC catalysts and that in PNP–Cu and ss–PNF–Cu precursors. However, further increasing Cu loading in PDA-based precursors reduces Cu content in CuNC, due to the formation of significant amounts of Cu nanoparticles in raw CuNC160 samples (Supplementary Figs. S11, S12 and Supplementary Table 3). These results demonstrate the crucial role of Cu^{2+} loading in the metal carrier in steering Cu content in Cu SACs. Compared with the CuNC160
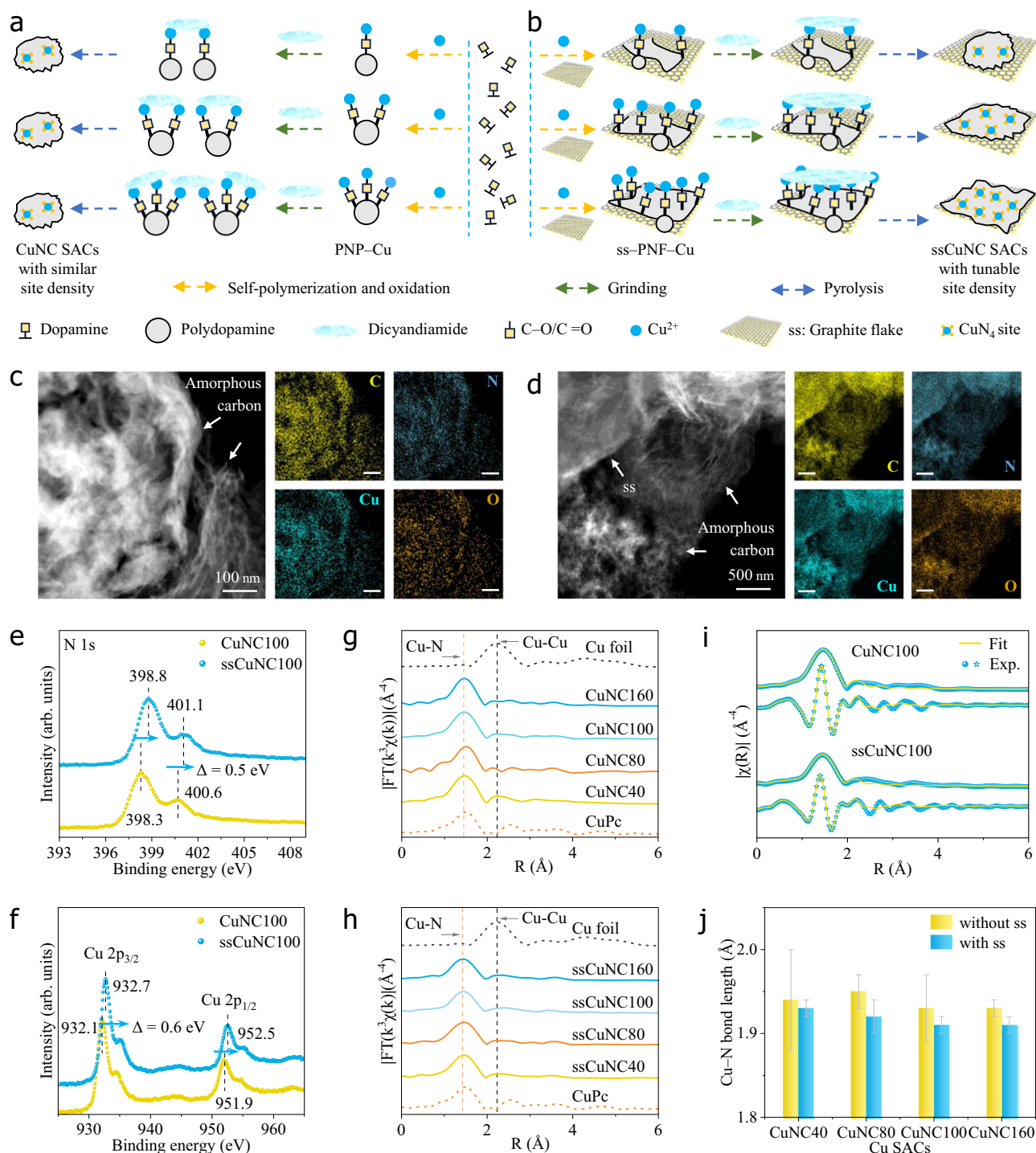
Fig. 1 | Support geometry engineering strategy and characterisation of the morphology, chemical, and electronic structures of ssCuNC and CuNC. Schematic of the synthesis of (**a**) CuNC and (**b**) ssCuNC via support engineering. DCD dicyandiamide, PNP–Cu Cu-chelated polydopamine nanoparticles, ss–PNF–Cu Cu-bound polydopamine nanoparticles and films coated on ss. HAADF-STEM images with EDS mapping of C (yellow), N (blue), Cu (cyan) and O (tan) for **c** CuNC100 and **d** ssCuNC100. **e** N 1s and **f** Cu 2p XPS core spectra of ssCuNC100 and CuNC100. k3-weighted R-space Cu K-edge EXAFS spectra of (**g**) CuNC and (**h**) ssCuNC. **i** Cu K-edge EXAFS fitting in R space of CuNC100 and ssCuNC100. Simulated (Fit, yellow) curves are superimposed on experimental (Exp., blue) dots. Each spectrum contains the k3-weighted magnitude (dots) and real part (stars) of χ(R). **j** Average Cu−N bond lengths of CuN$_4$ sites in CuNC and ssCuNC. Error bars represent one standard deviation from three independent trials. Source data are provided as a Source data file.

catalyst, the reduced formation of Cu nanoparticles and increased Cu loading in ssCuNC160 suggest that support engineering for CuNC using flat ss enhances Cu single atomisation in CuNC.

The Cu loadings of ssCuNC catalysts are found to be lower than those of CuNC catalysts because the weight of pure ss is included in the sample weight during ICP-MS quantification. In fact, XPS analysis reveals that the Cu and N contents (atomic percentage, at.%) on the surfaces of ssCuNC100 and ssCuNC160 are higher than those on CuNC100 and CuNC160 (Fig. 1e, f, Supplementary Figs. S13, S14 and Supplementary Table 4). In contrast to the relatively constant Cu and N contents in CuNC catalysts, the significant variation in Cu and N contents in ssCuNC further confirms the enhanced tunability of Cu

content in ssCuNC catalysts (Supplementary Fig. S14). This finding is partly because planar PNF, with lower curvature than spherical PNP, promotes uniform site distribution and close contact between PNF and DCD, resulting in a gradient increase in Cu site density with Cu ion concentration. These observations are consistent with the concept that support geometry engineering applied to the Cu carrier results in Cu SACs with enhanced tunability in site density, as depicted in Fig. 1a, b.

The single-atom nature of Cu sites in the as-prepared Cu SACs was investigated. High-angle annular dark-field scanning transmission electron microscopy (HAADF-STEM) coupled with energy-dispersive X-ray spectroscopy (EDS) mapping displayed uniform dispersion of C, O, N, and Cu across all CuNC and ssCuNC SACs (Fig. 1c, d, Supplementary Figs. S15–S18). The coordination environment and chemical states of Cu sites were confirmed by electron energy loss spectroscopy (EELS), X-ray spectroscopy, and fitting analysis. EELS data imply that the Cu–O moiety contributes negligibly to the local coordination environment in the representative CuNC100 and ssCuNC100 catalysts (Supplementary Fig. S19). Extended X-ray absorption fine structure (EXAFS) spectroscopy plots in R space for all ssCuNC and CuNC SACs display a main peak at ~1.45 Å, attributed to the Cu–N shell (Fig. 1g, h and Supplementary Table 5)[32,33]. EXAFS results also confirmed that no Cu–Cu bonds were detected in any Cu SACs, consistent with results from patterns, TEM images, selected area electron diffraction (SAED) patterns, and scanning electron microscopy (SEM) images (Supplementary Note 1).

To reveal the local structure of Cu SACs, comprehensive fitting analyses were carried out on Fourier-transformed EXAFS spectra in both radial (R) and wave vector (k) spaces. A single Cu–N scattering path and mixed scattering paths (including Cu–N/O, Cu–N/Cu, and Cu–N/O/Cu combinations) were used (Fig. 1i, Supplementary Figs. S20–S23). Supplementary Table 5 summarizes fitting parameters for the Cu SACs of interest, where the coordination number (CN) of N ranges from 3.8 to 4.3, with Cu–N bond length between 1.91 Å and 1.95 Å. The shortened or elongated Cu–N bond lengths suggest geometric distortion in Cu SACs, further supported by the geometric curvature observed in TEM images (see the following section). The fitting data also suggest that the Cu sites adopt a planar CuN_4 structure. Note that the average Cu–N bond lengths in ssCuNC are shorter than those in CuNC counterparts, indicating improved binding strength between single Cu atoms and primary supports, which stabilizes the isolated Cu sites in ssCuNC catalysts against demetallation and sintering (Fig. 1j). These results suggest that Cu sites feature single atomic distribution, and the isolated Cu site (CuN_4) are coordinated with an average of four N atoms in both ssCuNC and CuNC SACs.

The chemical states of Cu in the Cu SACs were also studied using XPS and X-ray absorption near edge structure (XANES) spectroscopy. Compared with CuNC catalysts, ssCuNC counterparts exhibit higher N 1s and Cu 2p binding energies, along with the lower C 1s binding energies. This finding demonstrates strong interactions between CuNC and ss in ssCuNC catalysts, leading to charge transfer from CuNC to ss and a higher oxidation state of Cu in ssCuNC compared to CuNC (Fig. 1e, f, Supplementary Fig. S13)[34,35]. The larger blue shift of the Cu 2p peak compared to the N 1s peak is attributed to the greater electronegativity difference between Cu and N. The average oxidation state of Cu in the Cu SACs was also quantified by XANES analyses via linear combination fitting (Supplementary Fig. S24)[36–38]. Results show that the Cu valence in both CuNC and ssCuNC catalysts decreases with increasing Cu loading, due to electronic interactions between neighbouring sites induced by the d_{site} effect. Thus, engineering the geometry of PDA-based supports using ss not only governs Cu contents in Cu SACs but also shortens the Cu–N bond length and improves the oxidation state of Cu in Cu SACs.

## Quantitative comparison of the d_{site} effect in ssCuNC and CuNC SACs

The effect of support geometry engineering on the d_{site} effect in Cu SAC was investigated. The average d_{site} value was calculated via statistical analysis of aberration-corrected (AC)-HAADF-STEM images for all catalysts. Each measured d_{site} value, as a statistical sample, refers to the shortest distance between a selected atom and its neighbour atom. AC-HAADF-STEM images of CuNC and ssCuNC catalysts show Cu atoms as bright spots with an average size of ~0.2 nm on the carbon substrate (Fig. 2a–h). The statistical average d_{site} values for the Cu catalysts were 2.2 nm (ssCuNC40), 0.93 nm (ssCuNC80), 0.68 nm (ssCuNC100), 0.36 nm (ssCuNC160), 0.89 nm (CuNC40), 0.85 nm (CuNC80), 0.81 nm (CuNC100), and 0.79 nm (CuNC160) (Fig. 2, Supplementary Figs. S25, S26 and Supplementary Table 6). Examination of STEM images showed a similar density of active Cu atoms in each CuNC catalyst. However, site densities in ssCuNC catalysts exhibited a progressive increase with Cu loading.

Structural distortions of Cu SACs were also studied via TEM characterization. CuNC SACs with similar Cu loadings exhibit comparable high substrate curvatures (Fig. 2I–IV and Supplementary Fig. S27a–d). In contrast, the substrate curvature of ssCuNC SACs increases progressively with increasing Cu loading (Fig. 2V–VIII and Fig. S27e–h). This finding indicates that Cu SACs with high site density or low d_{site} are more prone to inducing structural distortions. Note that the substrate of CuNC exhibits a distinctive discrete island-shaped distribution, whereas that of ssCuNC exhibits a continuous ribbon-shaped pattern (Supplementary Fig. S27). This difference in substrate geometry between CuNC and ssCuNC is closely related to the geometric differences in Cu-chelated PDA precursors used to synthesise CuNC and ssCuNC. Specifically, the former uses discrete Cu-chelated PDA nanoparticles (PNP–Cu), while the latter uses integrated Cu-chelated PDA nanoparticles and films conformally coated on ss (ss–PNF–Cu) (Fig. 1a, b, Supplementary Figs. S1, S3). During mixing of Cu-chelated PDA precursors with DCD to prepare Cu SACs, the larger-scale, continuous, planar ss–PNF–Cu with significantly lower curvature than spherical PNF–Cu, facilitates uniform Cu atoms distribution and provides substantial Cu atoms for direct interaction with DCD. Due to the high curvature of spherical PNF–Cu nanoparticles, a significant portion of Cu atoms within PNF–Cu fail to interact with DCD. Furthermore, compared to the uniform geometry of spherical PNP–Cu precursors, the varied geometry combinations of spherical PNP–Cu and planar Cu-chelated PDA films in ss–PNF–Cu precursors promote diverse interactions between Cu atoms and DCD. This phenomenon not only explains the heterogeneous site density in ssCuNC SACs and relatively consistent Cu site density in CuNC SACs with increasing Cu^{2+} concentration but also rationalizes the Cu site-density/d_{site}-dependent ECM performance shown in Fig. 3 (Fig. 2i and Supplementary Table 6). These findings are again consistent with the concept of an optimized d_{site} effect induced by support geometry engineering (Fig. 1a, b).

To correlate the d_{site} value with Cu site density on the catalyst surface, Cu site densities (n_s, Cu atoms per 100 nm^2) were calculated from STEM image statistics. The variation trend of n_s values is analogous to that of d_{site} values, with all CuNC catalysts exhibiting minimal differences (55–79), whereas ssCuNC catalysts show a broader n_s distribution (15–339, Supplementary Table 6). For a d_{site} value of ~0.7, the corresponding n_s of ssCuNC100 (112.5) is over 1.4 times larger than that of all CuNC catalysts, indicating that the activity of ssCuNC100 is supposed to be superior to that of all CuNC catalysts (Fig. 2j). The higher n_s values in ssCuNC compared to CuNC are partly attributed to enhanced anti-sintering ability, which is triggered by shorter Cu–N bond lengths (Supplementary Table 5). Figure 2k shows that d_{site} values and Cu loading in ssCuNC catalysts can be controlled over a significantly wider range than in CuNC catalysts.

The effect of the support on the charge conductivity of Cu SACs was also examined via electrochemical impedance spectroscopy (EIS) to compare the charge transfer resistances (R_{CT}) of CuNC and ssCuNC SACs (Supplementary Fig. S28). CuNC SACs exhibit a volcano-shaped trend in R_{CT}, with CuNC100 showing the lowest R_{CT}, while R_{CT} values for ssCuNC SACs decrease with increasing Cu loading (Supplementary Fig. S28c, d and Supplementary Table 3). R_{CT} values of both CuNC and ssCuNC SACs show a consistent negative correlation with Cu loading.
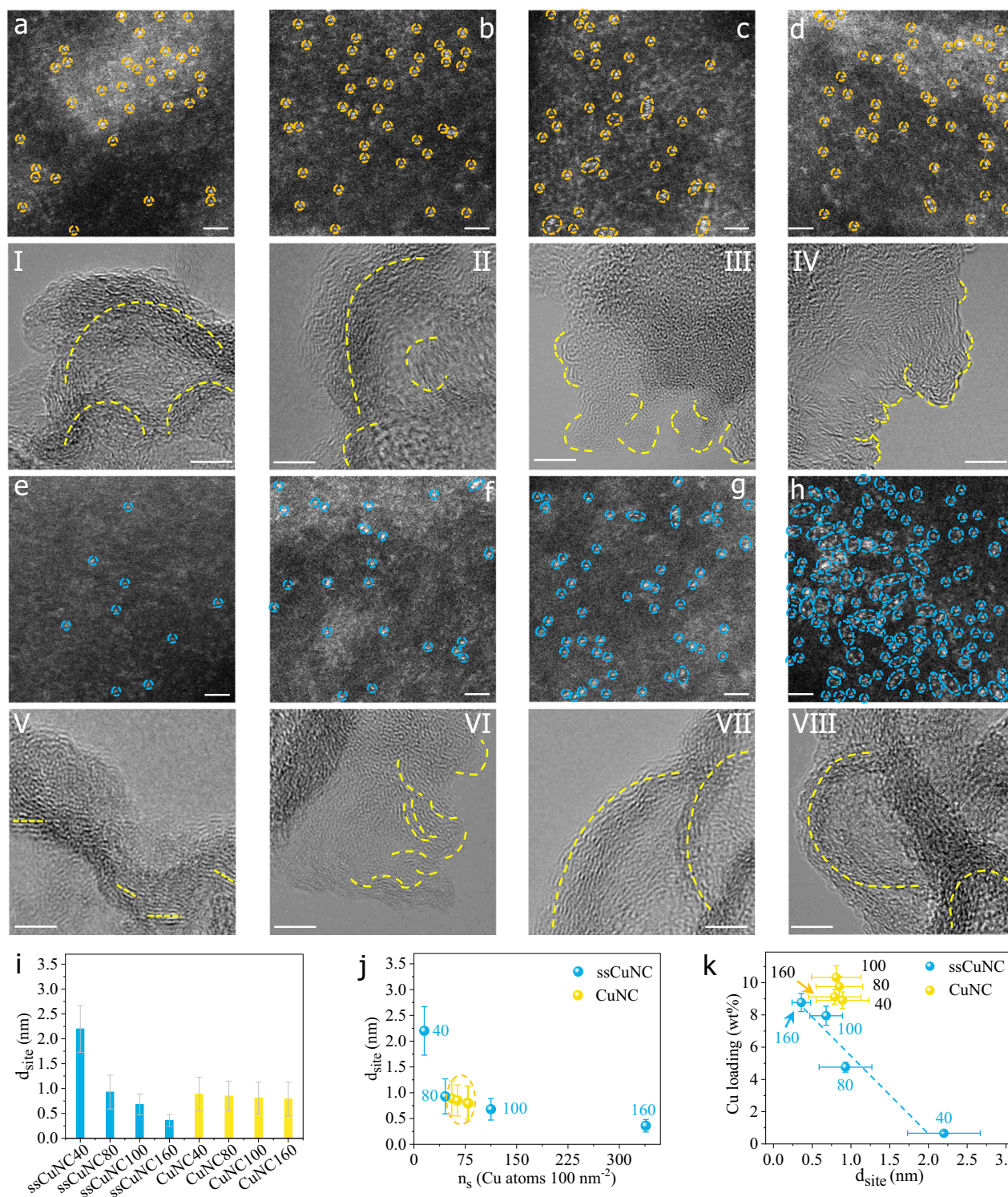
Fig. 2 | Correlation of the d_{site} effect with Cu loading in ssCuNC and CuNC SACs. AC-HAADF-STEM (**a–h**) and TEM (**I–VIII**) images of CuNC40 (**a, I**), CuNC80 (**b, II**), CuNC100 (**c, III**), CuNC160 (**d, IV**), ssCuNC40 (**e, V**), ssCuNC80 (**f, VII**), ssCuNC100 (**g, VIII**), and ssCuNC160 (**h, VIII**). Scale bars in (**a–h**) and (**I–VIII**) are 1 nm and 5 nm, respectively. Yellow dashed curves in (**I–VIII**) represent the degree of structural distortion in CuNC and ssCuNC. **i** d_{site} values determined from STEM images statistics. **j** Correlation between d_{site} values and site densities (n_s, Cu atoms per 100 nm²) calculated from STEM images statistics. **k** Relationship between d_{site} and Cu content measured by ICP-MS. Error bars in (**i–k**) represent one standard deviation for each sample synthesized in three independent trials. ssCuNC40, ssCuNC80, ssCuNC100 and ssCuNC160 were denoted by blue numbers 40, 80, 100 and 160 in (**j**) and (**k**); CuNC40, CuNC80, CuNC100 and CuNC160 are denoted by black numbers 40, 80, 100 and 160 in (**j**) and (**k**). Source data are provided as a Source data file.

This suggests a significant effect of Cu loading/site density of Cu SACs on charge transfer. Compared with other Cu SACs, the significantly higher Rct value of ssCuNC40 is mainly attributed to reduced CuNC coverage on graphite flakes and lower Cu loading (Supplementary Figs. S3, S8 and Supplementary Table 3). Excluding ssCuNC40, the

comparable R_{CT} values between CuNC and ssCuNC SACs rule out a dominant effect of ss on the charge transfer capability of Cu SACs. These findings evidence the crucial role of support geometry engineering in effectively controlling d_{site}, n_s, Cu loading, local structural distortion and charge conductivity in the as-prepared Cu-based catalysts.
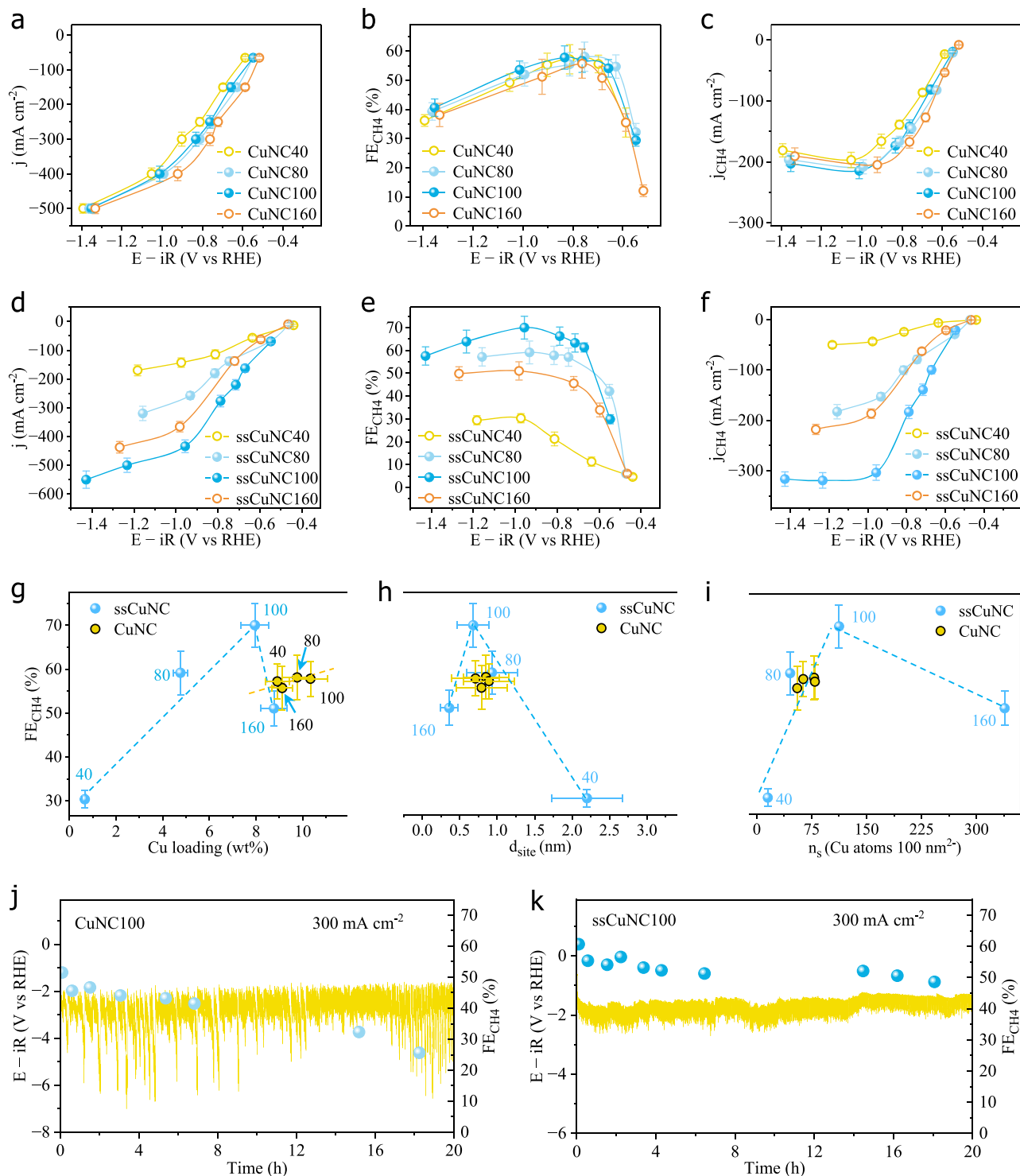
Fig. 3 | Comparison of ECM performances between ssCuNC and CuNC SACs. Total current density (j, **a**, **d**), FE_{CH4} (**b**, **e**) and CH₄ partial current density (j_{CH4}, **c**, **f**) for CuNC (**a**–**c**) and ssCuNC (**d**–**f**) SACs. Correlations of optimal FE_{CH4} with Cu loading (**g**), d_{site} (**h**) and n_s (**i**). All current densities are normalized by geometric area. Error bars in (**a**–**i**) represent one standard deviation from three independent samples. These measurements were conducted in a flow cell with 1 M KOH as the supporting electrolyte. ECM stability measurements for CuNC100 (**j**) and ssCuNC100 (**k**), performed at a constant current density of 300 mA cm⁻² in a flow cell with 1 M KHCO₃ as the supporting electrolyte. The measured resistance (R, where OCP: open circuit potential) used for the CuNC40-160, and ssCuNC40-160 electrodes in (**a**–**f**) was 2.3 ± 0.13, 2.6 ± 0.19, 2.4 ± 0.15, 2.1 ± 0.22, 2.0 ± 0.17, 2.4 ± 0.14, 2.2 ± 0.27, and 2.3 ± 0.14 Ω, respectively. The R was used for (**j**) and (**k**) was 5.3 ± 0.23, and 3.6 ± 0.26 Ω, respectively. Source data are provided as a Source data file.

ECM performance

ECM performance evaluation on Cu SACs with different d_{site} effects was conducted in a flow cell with a gas diffusion electrode (GDE) using 1 M KOH as the supporting electrolyte (used throughout this study)[4]. Catalysts were drop-cast on a GDE with a loading of ~0.2 mg cm^{-2}. ECM activities of ss, pure NC, ss-supported NC (ssNC), and ssNC modified with Cu nanoparticles (CuNPs/ssNC) were also investigated as control experiments (Supplementary Figs. S29 and S30). The sole product H$_2$ generated on ss, NC, and ssNC under high reductive current densities rules out ECM activity contributions from both ss and NC substrates (Supplementary Fig. S29 and Methods). CuNPs/ssNC exhibits an optimal Faradaic efficiency (FE) towards CH$_4$ (FE$_{CH4}$) of 36% at −1.4 V (Supplementary Fig. S30). This finding implies that dense Cu sites with the lowest d_{site} or highest n_s have limited selectivity toward CH$_4$, due to the competing carbon-carbon coupling reaction pathway on metallic Cu catalyst[11,12]. We then evaluated the ECM performance of CuNC catalysts. The total current density (j), CH$_4$ selectivity, and partial current density of CH$_4$ (j_{CH4}) for each CuNC catalyst exhibited minor changes as the applied potentials (all referenced to the reversible hydrogen electrode (RHE)) became increasingly negative (Fig. 3a–c). Specifically, the optimal FE$_{CH4}$ values for CuNC40, CuNC80, CuNC100 and CuNC160 were 57% at −0.81 V, 58% at −0.75 V, 58% at −0.83 V and 56% at −0.76 V, respectively (Fig. 3b and Supplementary Fig. S31a–c, g). The peak j_{CH4} values for CuNC40, CuNC80, CuNC100 and CuNC160 was 196.8 mA cm^{-2} at −1.1 V, 208.0 mA cm^{-2} at −1.0 V, 214.4 mA cm^{-2} at −0.97 V, and 204.8 mA cm^{-2} at −0.92 V, respectively (Fig. 3c).

In contrast, ssCuNC catalysts showed significant variations in ECM kinetics, with ssCuNC100 exhibiting the highest j and j_{CH4} across all applied potentials (Fig. 3a, c, d, f). A similar trend is observed in the variation of FE$_{CH4}$ for ssCuNC catalysts (Fig. 3e and Supplementary Fig. S31d–f, h). The optimal FE$_{CH4}$ of ssCuNC100 (70% at −0.96 V) is at least 10% higher than that of all CuNC and other ssCuNC catalysts (30% for ssCuNC40 at −0.97 V, 59% for ssCuNC80 at −0.93 V, and 51% for ssCuNC160 at −0.98 V). At ~−1.0 V, j_{CH4} of ssCuNC100 (303.9 mA cm^{-2}) is 7.0-, 2.0-, 1.6-, and ~1.5-fold higher than that of ssCuNC40 (43.3 mA cm^{-2}), ssCuNC80 (152.9 mA cm^{-2}), ssCuNC160 (186.7 mA cm^{-2}), and CuNC catalysts, respectively (Supplementary Fig. S32). The effect of electrochemical surface area (ECSA) on ECM performance was also evaluated via cyclic voltammetry measurements for Cu SACs in an Ar-saturated 1 M KOH electrolyte using a flow cell setup (Supplementary Fig. S35 and Supplementary Table 7). The optimal j_{CH4} after ECSA normalization (j_{CH4_ECSA}) was further examined. The optimal j_{CH4_ECSA} values for CuNC40, CuNC80, CuNC100, CuNC160, ssCuNC40, ssCuNC80, ssCuNC100, and ssCuNC160 were 0.67, 0.65, 0.72, 0.67, 0.44, 0.71, 1.3, and 0.57 mA cm^{-2}, respectively. These j_{CH4_ECSA} values show a similar trend to those determined by geometric area, as shown in Fig. 3. This finding rules out a predominant effect of ECSA on ECM performance. Thus, these differences in ECM performance between CuNC and ssCuNC indicate that support geometry engineering effectively enhances the selectivity and activity of CuNC over a wider range.

To reveal the origin of performance differences between CuNC and ssCuNC, the correlation between ECM selectivity/activity and the d_{site} effect of Cu catalysts was investigated. The correlation of FE$_{CH4}$ with Cu loading shows that optimal FE$_{CH4}$ depends on Cu loading across all Cu specimens, particularly for ssCuNC (Fig. 3g). However, all CuNC catalysts with higher Cu loadings exhibit lower CH$_4$ selectivity than ssCuNC80 and ssCuNC100, suggesting that Cu loading is not crucial for determining CH$_4$ selectivity in Cu SACs. Figure 3h and Fig. 3i, respectively, display a volcano-shaped trend relating optimal FE$_{CH4}$ to d_{site} and optimal FE$_{CH4}$ to n_s, with the highest CH$_4$ selectivity observed at a d_{site} of 0.68 nm and an n_s of 112.5 Cu atoms per 100 nm^{-2}. Note that CuNC catalysts with similar optimal FE$_{CH4}$ values have a similar d_{site} of 0.8–0.9 nm or an n_s of 60 ~ 80 Cu atoms per 100 nm^2. Furthermore, the optimal FE$_{CH4}$ of ssCuNC100 is much higher than that of CuNC160 despite their similar d_{site}, due to the higher n_s of

ssCuNC100 relative to CuNC160 (Fig. 3i and Supplementary Table 6). A correlation analysis of j_{CH4} (at ~−0.1 V) with Cu loading, d_{site} and n_s yielded similar conclusions to those discussed above (Supplementary Fig. S32). These results, coupled with the linear relationship between FE$_{CH4}$/j_{CH4} and n_s, suggest that Cu site density is a crucial descriptor for ECM selectivity and activity on Cu SCAs. The relationship between the d_{site} effect and ECM activity described above was also verified using ssCuNC100 (denoted as ssCuNC100-scale-up) prepared via a scale-up synthesis procedure (see Methods). The synthesized ssCuNC100-scale-up SAC shows a similar Cu-site coordination environment and d_{site} effect, achieving an optimal FE$_{CH4}$ of 68% at −0.96 V (Supplementary Figs. S33, S34 and Supplementary Table 5). The comparable structure-activity relationship observed for both ssCuNC100 and ssCuNC100-scale-up further confirms the scalability of our synthesis strategy.

The effect of electrolyte pH on ECM for CuNC100 and ssCuNC100 SACs was investigated. CO$_2$RR electrolysis using CuNC100 and ssCuNC100 SACs was conducted in a liquid-flow electrolyser with 1 M KHCO$_3$ electrolyte. Results showed that the optimal FE for CH$_4$ production was 49.8% for CuNC100 and 59.2% for ssCuNC100 at 300 mA cm^{-2}, respectively (Supplementary Fig. S31i, j). These values are ~10% lower than those obtained in 1 M KOH, which is attributed to suppressed hydrogen evolution reaction (HER) in alkaline environments, as is evidenced by the lower FE of H$_2$ formation detected in 1 M KOH electrolyte (Supplementary Fig. S31g, h). ECM stability measurements using CuNC100 and ssCuNC100 were conducted at a current density of 300 mA cm^{-2} in a flow cell with 1 M KHCO$_3$ as the supporting electrolyte. ssCuNC100 displays stable CH$_4$ production, with FE remaining above 50% over 20 h. In contrast, the FE for CH$_4$ formation on CuNC100 rapidly decreased from ~42% at 6 h to 25% at 18 h (Fig. 3j, k). The stability difference between CuNC100 and ssCuNC100 was further studied via spectroscopy analysis.

Spectroscopic investigations

To investigate the relationship between ECM performance and the d_{site} effect for ssCuNC and CuNC, we examined the selectivity of combined C$_2$ products (ethylene, acetate and ethanol) and carbon monoxide (CO) as a function of applied potential (Fig. 4a, b). CO is a crucial intermediate for hydrocarbon production. Figure 4a shows that the FE$_{CO}$ of ssCuNC100 is lower than that of CuNC100 across all applied potentials. This FE$_{CO}$ trend was also observed for other CuNC and ssCuNC catalysts (Supplementary Fig. S36a–c). In contrast, FE$_{C2}$ is higher for CuNC100 than for ssCuNC100 under the same conditions. Note that FE$_{C2}$ (<15%) on ssCuNC160 at high j exceeds that on CuNC160, which is ascribed to improved carbon-carbon coupling activity on highly dense Cu sites (Supplementary Fig. S36f). Product distribution analysis suggests that ssCuNC enables a higher degree of CO$_2$ hydrogenation to CH$_4$ at the expense of more CO than CuNC.

We further investigated the origin of improved CO$_2$-to-CH$_4$ selectivity on ssCuNC at the molecular level using in situ attenuated total reflection Fourier-transform infrared spectroscopy (ATR-FTIR), with ssCuNC100 and CuNC100 as model catalysts. Four regions of interest, identified at 2120–2070 cm^{-1}, 1750–1640 cm^{-1}, 1640–1475 cm^{-1} and 1470–1398 cm^{-1}, are associated with linearly adsorbed *CO (v(*CO$_L$)), stretching vibrations of H$_2$O (δ(H$_2$O)), strongly adsorbed *CO$_2$ (v(*CO$_2$)), and *OCH$_3$ adsorbed at the ssCuNC100 and CuNC100 interfaces, respectively (Fig. 4c, d)[39–42]. The band associated with *OCH$_3$ adsorbed at atomic CuN$_4$ site is also confirmed via computational simulation (Supplementary Fig. S37). The δ(H$_2$O) and v(*CO$_2$) bands show potential-dependent positive and negative peaks. Both peak intensities increase with applied potential, with those in ssCuNC100 being significantly stronger than those in CuNC100. These results suggest rapid consumption of adsorbed *CO$_2$ and a higher mass transfer rate on ssCuNC100 than on CuNC100, accounting for the enhanced ECM activity of ssCuNC100 relative to CuNC100.
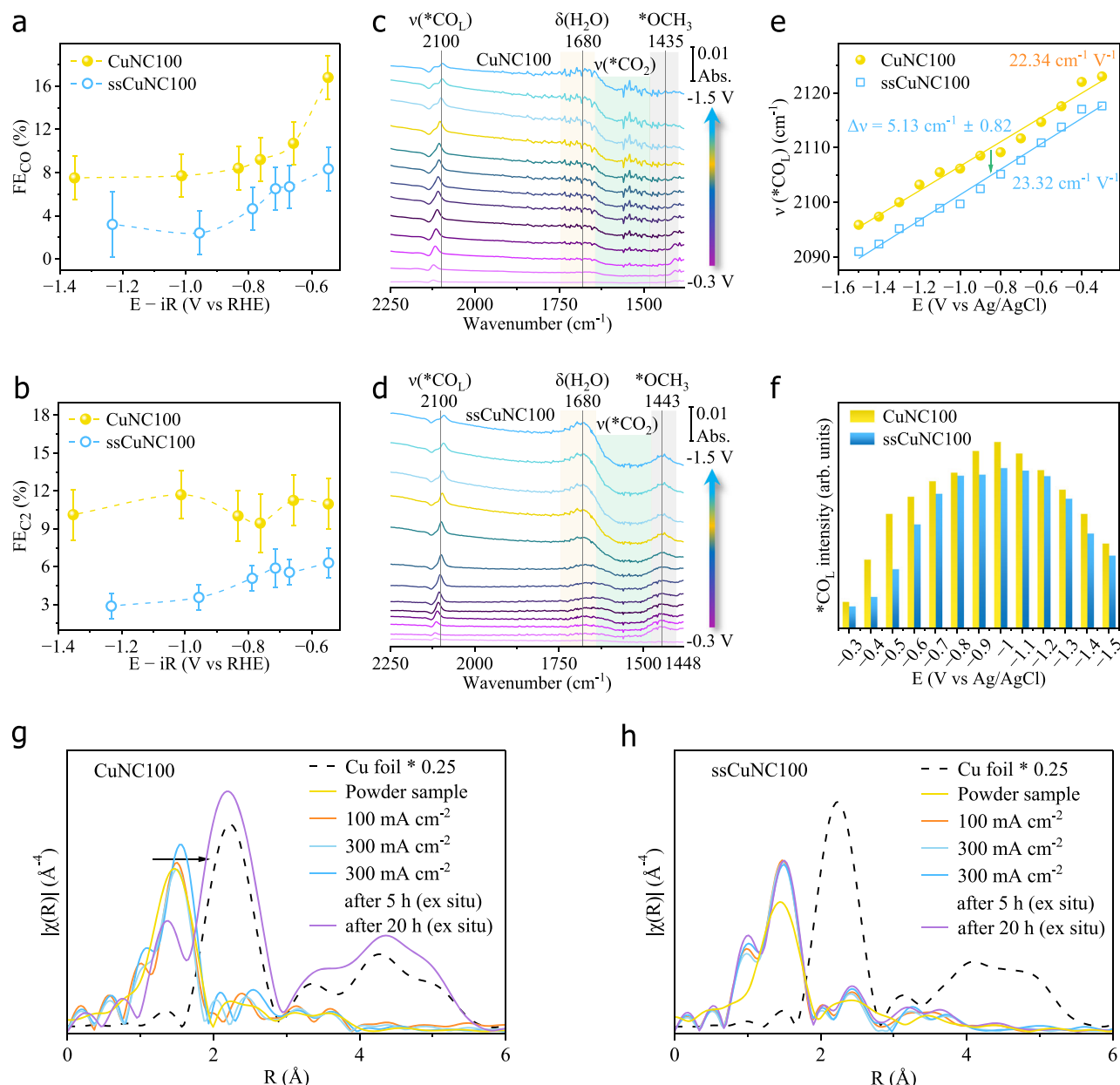
Fig. 4 | Relationship between ECM selectivity and adsorbed intermediates on ssCuNC100 and CuNC100 SACs. FE for CO (**a**) and C_2 products (ethylene, acetate and ethanol) (**b**) at different applied potentials. Error bars represent one standard deviation from three independent samples. The R used for CuNC100 and ssCuNC100 in (**a**, **b**) was 2.4 ± 0.15 and 2.2 ± 0.27 Ω, respectively. In situ ATR-FTIR spectra of CuNC100 (**c**) and ssCuNC100 (**d**) SACs under different applied potentials. **e** Stark effect of linearly adsorbed CO (*CO_L) vibration as a function of potential. **f** *CO_L intensity as a function of potential. *CO_L wavenumbers and intensities in (**e**) and (**f**) were derived from spectra (**c**) and (**d**). *: Denotes active reaction sites. In situ and ex situ Cu K-edge EXAFS spectra of CuNC100 (**g**) and ssCuNC100 (**h**) under different applied current densities. Source data are provided as a Source data file.

The peak positions of ν(*CO_L) in both ssCuNC100 and CuNC100 shifted to lower wavenumbers as the applied potential became more negative, showing a Stark effect (Fig. 4e)[43]. Over the entire potential range of −0.3 to −1.5 V, ssCuNC100 displayed a lower wavenumber than CuNC100 and a higher Stark tuning rate (23.3 cm^{-1} V[-1]) in comparison to CuNC100 (22.3 cm^{-1} V[-1]), indicating a stronger interaction between *CO_L and ssCuNC100[41]. This interprets the suppressed CO liberation on ssCuNC100. Under identical CO_2 electrolysis conditions, the intensity of *CO_L on CuNC100 exceeds that on ssCuNC100, suggesting higher *CO coverage on CuNC100 and thus accounting for the increased C_2 production observed on CuNC100 (Fig. 4b, f). The reduced *CO coverage and improved peak intensity of

the *OCH_3 band on ssCuNC100 also indicate favourable hydrogenation of *CO to form *OCH_3 at the expense of *CO on ssCuNC100 (Fig. 4c, d, f). This hydrogenation process is identified as the dominant selectivity-determining step in CH_4 production[3,40].

To elucidate the effect of structural alterations of active sites on ECM performance, we carried out in situ and ex situ XAS measurements and analyses for ssCuNC100 and CuNC100 SACs under different current densities (Supplementary Figs. S38–S43, Supplementary Table 8; See Methods). Both in situ and ex situ R-space Cu K-edge EXAFS spectra show a positive shift of the main peak, which—based on fitting results—is attributed to an increase in Cu−N bond lengths for both CuNC100 and ssCuNC100 during CO_2RR (Fig. 4g, h). Specifically,
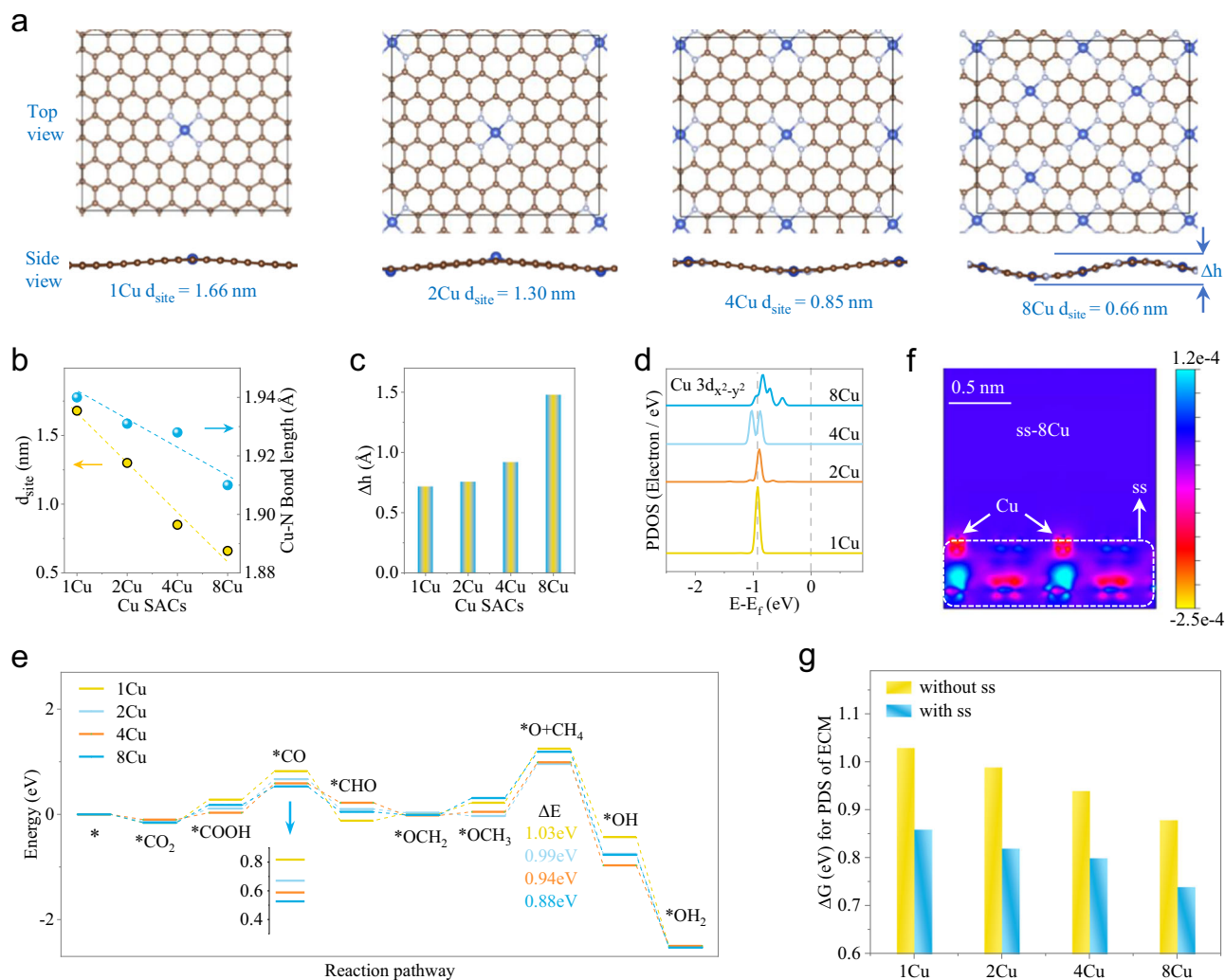
Fig. 5 | Identification of d_{site} effect-induced structure and coordination environment in Cu SACs. a Optimized atomic CuN_4 structure (upper: top view; lower: side view) for 1Cu, 2Cu, 4Cu and 8Cu SACs with d_{site} of 1.68, 1.3, 0.85 and 0.66 nm, respectively. blue, brown, and silver-grey balls represent Cu, C, and N atoms, respectively. **b** Correlation of d_{site} (left) and Cu−N bond length (right) with different Cu SACs. **c** Relationship between the height difference (Δh) of the distorted graphene layer (see bottom part in (**a**)) and different Cu SACs. **d** Partial density of states (PDOS) projected onto Cu $3d_{x^2-y^2}$ orbitals. **e** Free energy profile for the CO_2-to-CH_4 pathway at the active CuN_4 site. Inset: Adsorption energy of *CO. ΔE: Free energy change for protonation of *OCH_3 to *$O + CH_4$ on the CuN_4 site. **f** Charge density difference with 2D cross-sectional view (red/blue regions: electron accumulation/depletion) of ss-engineered 8Cu (ss-8Cu) interface structures. **g** Free energy plot of the potential-determining step (PDS) for CO_2-to-CH_4 on Cu SACs (yellow bars) and ss-engineered Cu SACs (blue bars), ss: Secondary support. Models incorporating ss are presented in Supplementary Fig. S52a. Source data are provided as a Source data file.

during 5 h of CO_2RR, the Cu−N bond length of CuNC100 increased significantly from 1.93 Å to 1.96 Å, 0.03 Å longer than the Cu−N bond length of ssCuNC100 (1.93 Å). This finding implies more pronounced geometric structure distortion of CuN_4 sites in CuNC100 compared to those in ssCuNC100 during CO_2RR. After 20 h of CO_2RR, the Cu−N bond length of CuNC100 recovered to 1.94 Å, still 0.01 Å longer than that of ssCuNC100 (1.93 Å). Note that a new peak assigned to Cu−Cu bond emerged in CuNC100. These results indicate that active sites in ssCuNC100 remained as single-site CuN_4 structures, whereas those in CuNC100 transformed from single-site CuN_4 structures to a combination of CuN_4 and metallic Cu after 20 h of CO_2RR. This phenomenon rationalizes the observed differences in ECM performance between CuNC100 and ssCuNC100, as depicted in Fig. 3. Thus, in situ and ex situ XAS results offer direct experimental evidence that CuN_4 is the active site in Cu SACs for ECM and that the Cu−N bond in ssCuNC100 is more stable against structure distortion than that in CuNC100 during ECM. This also accounts for the lower defect density in the ssCuNC100 framework relative to that in CuNC100 (Supplementary Fig. S44).

Theoretical study using density functional theory calculations

We further performed density functional theory (DFT) calculations to understand the origin of catalytic CO_2-to-CH_4 activity on Cu SACs with different d_{site} values. Decreasing d_{site} from 1.68 nm (1Cu) to 0.66 nm (8Cu) shortens the average Cu−N coordination bond length from 1.94 Å to 1.91 Å, consistent with XAS fitting results for Cu SACs (Fig. 5a, b, Supplementary Table 5 and Supplementary Data 1). Concurrently, the interlayer height difference (Δh) increased from 0.72 to 1.48 Å (Fig. 5c), suggesting potential graphene twisting under dense CuN_4 motifs, which aligns with TEM observations (Fig. 2I-VIII, Fig. 5a and Supplementary Fig. S27). Electronic restructuring was evidenced by the splitting and upward shift of Cu $3d_{x^2-y^2}$ orbitals toward the Fermi level, elevating the d-band centre (Fig. 5d). This, in turn, changes their electron distribution, thereby influencing catalytic activity[44].

Supplementary Fig. S45 shows that the highest occupied orbital of planar four-coordinated Cu ions is $3d_{x^2-y^2}$, and the 2p orbitals of adsorbates hybridize to form bonding and antibonding orbitals. When the energy level of Cu $3d_{x^2-y^2}$ orbitals shifts to the Fermi level, the

antibonding orbitals also increase in energy[45,46]. Accordingly, the number of electrons in the antibonding orbitals decreases, strengthening the bonding and enhancing the adsorption capacity of adsorbents at Cu sites[45]. This enhancement agrees with experimental results, where promoted CH_4 production is achieved at the expense of CO, accompanied by a stronger *CO adsorption signal on ss-engineered Cu SACs (Fig. 4c, d). Moreover, the increase in density of states (DOS) values at the Fermi level with increasing Cu loading indicates enhanced electron transfer kinetics between catalytic intermediates and high-density catalytic centres (Supplementary Fig. S46)[47]. This d_{site} effect establishes a distinct electron distribution at the Fermi energy level by modulating Cu 3d orbital splitting, thereby enhancing intrinsic ECM activity[48].

The DFT-based climbing-image nudged elastic band (CI-NEB) method was used to calculate kinetic barriers for Cu atom detachment from a CuN_4 SA site, subsequent defect formation, and cluster aggregation (Supplementary Fig. S47 and Supplementary Data 1). Calculations reveal that removing a Cu atom from ss-free CuNC requires an energy barrier of 3.68 eV, whereas ss-supported CuNC necessitates a higher energy of 4.02 eV. Furthermore, the defect formation energy of CuNC (2.47 eV) is lower than that of ssCuNC (2.87 eV). These results demonstrate enhanced structural stability of CuN_4 single-atom sites with ss incorporation. The suppression of Cu atom detachment is likely attributed to the stronger Cu−N bond (with shorter bond lengths in ssCuNC100, as confirmed by XAS) and optimized support geometry induced by ss. These findings align with experimental observations of reduced defect density, increased active site density, and enhanced electrochemical stability for the ssCuNC100 SAC.

To further clarify the effect of high-density CuN_4 sites on boosting CH_4 selectivity, we performed DFT calculations coupled with a computational hydrogen electrode (CHE) model. We elucidated the free energy diagram of the lowest-energy pathway for CO_2-to-CH_4 conversion at the active CuN_4 site, along with atomic configurations of each elementary step (Fig. 5e, Supplementary Fig. S48 and Supplementary Data 1). The potential-determining step (PDS) for CO_2-to-CH_4 conversion at the CuN_4 site involves protonation of *OCH_3 to *$O + CH_4$, requiring cleavage of the C−O bond in *OCH_3. The associated free energy change (ΔE) is 1.03 eV for the 1Cu catalyst, decreasing to 0.99, 0.94 and 0.88 eV for the 2Cu, 4Cu and 8Cu catalysts, respectively (Fig. 5e). In the explicit solvent model, where solvent molecules are included in calculations, the change in the energy barrier is more significant. Furthermore, the trend of the energy barrier change is consistent with results from the CHE model (Supplementary Figs. S49, S50 and Supplementary Data 1). These results indicate that the thermodynamic favourability of CH_4 production at the CuN_4 site enhances with increasing site density. Adsorption of the *CO intermediate promotes the formation of deep reduction products, including CH_4. Interestingly, high-density CuN_4 sites with a lower d_{site} value can stabilize *CO adsorption due to their relatively elevated d_{x2-y2} orbital level (Supplementary Fig. S45 and Fig. 5e, inset). For the competitive HER, the calculated free energies for HER on 1Cu, 2Cu, 4Cu, and 8Cu are 1.16, 1.40, 1.45, and 1.61 eV. In contrast, the Cu(100) counterpart (d_{site} of 0.26 nm) exhibits a significantly lower free energy of only 0.24 eV (Supplementary Fig. S51a). We further found that Cu(100) enables CO_2 adsorption and exhibits a comparably low free energy barrier (0.4 eV) for the C−C coupling PDS, indicating that Cu(100) offers extra active sites for the CO_2-to-C_2H_4 process (Supplementary Fig. S51b). These results suggest that protonation/deprotonation on different Cu SACs is considerable challenging, while agglomerated Cu sites exhibit superior HER and competitive C−C coupling activities, in line with CO_2RR performance observed for CuNPs/ssNC, CuNC and ssCuNC (such as ssCuNC160) SACs (Supplementary Figs. S30, S31, S36).

We also examined the charge density difference and adsorption free energies of reaction intermediates for ssCuNC SACs to explore the effect of ss on CuNC SACs. Examination of the charge density difference in ssCuNC reveals significant charge transfer from CuNC to ss (Fig. 5f, Supplementary Fig. S52 and Supplementary Data 1). This accounts for the positively charged Cu atoms found in both XPS and XAS results for ssCuNC SACs (Fig. S13 and Fig. S24). Compared to CuNC, ssCuNC exhibits a lower free energy barrier for the PDS of CO_2-to-CH_4 conversion, confirming that ss also helps improve CH_4 selectivity over CuN_4 sites (Fig. 5g). These findings show the versatile role of support engineering in tuning the d_{site} effect, coordination environment, chemical structure, and intrinsic reactivity of interacting sites in SACs.

Discussion

In summary, we report a support geometry engineering strategy to optimize the d_{site} effect and intrinsic electrocatalytic performance of active sites in SACs by tuning the binding strength between single metal atoms and a catalytically inert secondary support. Flat graphite was used as a secondary support and model to verify our method. Engineering PDA with ss leads to the formation of differentiated geometric combinations of spherical (particulate) and flat (film) PDA-based metal precursors, which are used to synthesise ss-engineered CuNC SACs. Strong interactions between CuNC and ss enable regulation of the Cu−N bond length. This strategy enables effective control of Cu loading, d_{site}, and n_s in Cu SACs over a wide range. Reducing d_{site} to -0.7 nm optimizes both the coordination environment and electronic structure of Cu sites, significantly enhancing their intrinsic ECM reactivity in Cu SACs.

We found that the d_{site} effect, particularly n_s, of Cu SACs plays a critical role in determining ECM selectivity and activity. Specifically, at ~-1.0 V, the ssCuNC SAC with a moderate d_{site} of 0.68 nm and an n_s of 112.5 Cu atoms 100 per nm^2 shows increased CH_4 selectivity of 70% and a j_{CH4} of 303.9 mA cm^{-2}, at least 1.5 times higher than that of all CuNC catalysts without ss. In-situ spectroscopic and computational studies confirmed that ssCuNC SACs with modified electron distribution and Cu−N bond length, show optimized d_{site} and n_s values. These modifications improve adsorption capacity, stabilize *CO adsorption, and favours cleavage of the C−O bond in *OCH_3, thereby promoting ECM selectivity and activity. This approach sheds light on the relationship between the support effect, the proximity effect of interacting metal sites, and the CO_2RR catalytic mechanism. It also provides guidance for developing highly efficient materials with tunable site densities and reactivities.

Methods

Chemicals and materials

Sigracet 28BC gas diffusion layer (28BC GDL, SGL Carbon, Germany); anion-exchange membranes (Fumasep FAA-3-PK-130 (thickness: 130 µm, FuMA-Tech BWT GmbH) was activated in a 0.5 M aqueous NaCl solution for 24 h, washed with water, and used in liquid-electrolyte flow cells. Sustainion X37-50 grade 60 (thickness: -50 µm, Dioxide Materials) was activated in a 1 M aqueous KOH solution for 48 h, washed with water, and used in membrane electrode assembly electrolysers); dimethyl sulfoxide (DMSO, ≥99.9%, Thermo Scientific, USA); deuteroxide (D_2O, 99.9%, Sigma-Aldrich, USA); aqueous ammonia solution (30 wt%, Macklin, China); dopamine hydrochloride (Sigma-Aldrich, Germany); anhydrous cupric sulfate ($CuSO_4$, Sigma-Aldrich, USA); Nafion solution (5 wt%, Sigma-Aldrich, Germany); 2-propanol (≥99.5%); absolute ethanol (≥99.0%). High purity (99.99%) CO_2, H_2, He, and Ar (Air Liquide, China); nickel plate (0.1 mm thick, Dongguan Shengze Metal Material Co., LTD., China). All chemicals were used as received. All aqueous solutions were prepared fresh as needed using deionized (DI, Milli-Q) water with a resistivity of 18 MΩ cm^{-1}, and all prepared solutions were stored in a refrigerator at -5 °C.

Synthesis of ss−PNF−Cu precursors (Cu-chelated polydopamine films and nanoparticles coated on ss): 0.2 g of graphite flake powder was added to a conical flask containing 90 mL of ultrapure water and

5 mL of ethanol (99.7%, Shanghai Lingfeng Chemical Reagent Co., Ltd., China) as solvents, followed by ultrasonication for 30 min. Next, 2 mL of ammonia solution (30 wt%) and 35 mL of ethanol (99.9%) were injected into the flask with stirring at 500 rpm. Subsequently, 10 mL of an aqueous solution containing dopamine hydrochloride (DAH) and $CuSO_4$ was added dropwise. The flask was sealed, and the mixture was stirred at 1500 rpm under ambient conditions for 24 h. The resulting black precipitate was collected by centrifugation at 12,000 rpm for 30 min, then dried overnight in a vacuum oven at 60 °C. The weight ratio of DAH to $CuSO_4$ is described in the "Synthesis of ssCuNCX (X = 40, 80, 100, 160) and CuNCX".

Scale-up synthesis of ss–PNF–Cu precursor (Supplementary Fig. S33a): 8.0 g of graphite flake powder was added to a reagent bottle containing 1.7 L of ultrapure water and 0.70 L of ethanol (99.7%) as solvents, followed by ultrasonication for 30 min. Next, 40 mL of ammonia solution (30 wt%) and 0.5 L of ethanol (99.9%) were injected into the bottle with stirring at 700 rpm. Then, 0.25 L of an aqueous solution containing DAH (10.0 g) and $CuSO_4$ (4.0 g) was added dropwise. The bottle was sealed, and the mixture was stirred at 700 rpm under ambient conditions for 24 h. The resulting black precipitate was collected by vacuum filtration and dried overnight in a vacuum oven at 60 °C. The remaining synthesis steps follow those described in "Synthesis of ssCuNCX (X = 40, 80, 100, 160) and CuNCX".

Synthesis of PNP–Cu precursors (Cu-chelated polydopamine nanoparticles): Precursors synthesis followed the same procedure as "Synthesis of ss–PNF–Cu precursors", except that no ss powder was added.

Synthesis of ssCuNCX (X = 40, 80, 100, 160) and CuNCX: ssCuNCX was prepared by uniformly mixing and grinding dry ss–PNF–Cu powder with dicyandiamide (DCD) at a weight ratio of 1:11. The ground powder was placed in a ceramic boat and transferred to a temperature-programmed furnace for pyrolysis under an inert gas stream. The pyrolysis program was as follows: (1) purge the furnace with high purity Ar gas at 50 SCCM for 40 min; (2) heat from room temperature to 800 °C at a ramp rate of 5 °C min^{-1}; (3) hold at 800 °C for 90 min; (4) cool naturally to room temperature. The resulting catalyst was ground, collected, and stored in an Ar-purged glove box at room temperature. ssCuNC160, ssCuNC100, ssCuNC80, and ssCuNC40 were prepared with DAH-to-$CuSO_4$ weight ratios of 0.25 g:0.16 g, 0.25 g:0.10 g, 0.25 g:0.08 g, and 0.25 g:0.04 g, respectively. The same procedure was used to synthesise the ssCuNC100-scale-up SAC, except that the controlled atmosphere box furnace (LC-SA3-20-12TP, LICHEN, China) was purged with high-purity Ar gas at 300 SCCM.

CuNCX catalysts (X = 40, 80, 100, 160) were synthesized using the same procedure, except that dry G–PNF–Cu powder was used instead of dry PNP–Cu powder.

Synthesis of ssNC (ss-supported N-doped carbons): ssNC was synthesised using the same procedures as "Synthesis of ss–PNF–Cu precursors" and "Synthesis of ssCuNCX", except that no $CuSO_4$ was added.

Synthesis of NC: NC was synthesised using the same procedures as "Synthesis of ssNC", except that no ss powder was added.

Synthesis of CuNPs/ssNC (ssNC modified with Cu nanoparticles): CuNPs/ssNC were synthesised using the same procedures as "Synthesis of ss–PNF–Cu precursors" and "Synthesis of ssCuNCX", except that no DCD was added.

Characterisation

Scanning electron microscopy (Thermofisher Apero 2 S HiVac), transmission electron microscopy (FEI-Talos F200S), and probe-corrected scanning transmission electron microscopy (Thermo-Fisher Themis Z, operating voltage: 300 kV) were used to characterize the morphology of the samples. Prior to collecting SEM images of PNP–Cu and G–PNF–Cu precursors, the samples were coated with a thin layer of platinum particles using a Quorum

EMS150TES Plus precision coating system. X-ray diffraction (XRD) patterns were recorded using a Bruker D8 ADVANCE X-ray powder diffractometer (Cu Kα radiation, λ = 0.15406 nm). Surface analysis of catalysts was performed using X-ray photoelectron spectroscopy (XPS) with a Thermo Scientific Escalab xi$^+$ system equipped with a focused monochromatic Al Kα X-ray source (hv = 1486.6 eV, 650 μm spot size). Survey scans (wide) and high-resolution scans (narrow) were recorded at analyser pass energies of 150 and 20 eV, with step sizes of 1.0 eV and 0.1 eV, respectively. All XPS data were calibrated against the C 1s peak at 284.8 eV unless otherwise specified. All X-ray absorption spectroscopy (XAS) measurements were conducted at the XAS Beamline of the Australian Synchrotron, ANSTO. A Si(111) double-crystal monochromator was used to monochromatize the white beam, and the energy resolution of the setup is approximately 0.2 eV at the Cu K-edge. A 36-element Canberra silicon drift detector (SDD) was used to collect the fluorescence signal. The beam was collimated to a vertical size of ~0.3 mm at the sample position. XAS spectra were collected at room temperature. For the pre-edge region, a 2 eV energy step with 1 s integration time per point was used. The X-ray absorption near-edge structure (XANES) region was scanned using a 0.2 eV step with the same dwell time. Extended X-ray absorption fine structure (EXAFS) data were collected up to k = 13 Å^{-1} with a variable energy step corresponding to $\Delta k \approx 0.05$ Å^{-1}. The integration time per point increased from 2 to 5 seconds as a function of k to improve data quality at high k values. For in-situ measurements, XAS spectra were recorded in slow-scan (continuous energy) mode, with a typical acquisition time of 5 min per scan. The in-situ electrochemical cell was fabricated from Polyetherketoneketone (PEKK). It employed nickel foam as the anode, a Hg/HgO reference electrode, and carbon paper as the cathode, with ~5.6 mg cm^{-2} of catalyst loaded onto the carbon paper (active area: 1 cm^2). The X-ray window was sealed with Kapton tape, and the total thickness of the cathode layer was 370-450 μm. EXAFS data processing was performed using the ATHENA module from the IFEFFIT software suite. The k^3-weighted χ(k) spectra were transformed from k-space (3–10.5 Å^{-1}) to R-space using a Hanning window with dk = 1.0 Å^{-1}. To extract quantitative structural information around Cu atoms, curve fitting of the R-space data was performed using the ARTEMIS module of IFEFFIT. Fitting parameters and additional details are provided in Supplementary Tables 5 and 8. For in-situ measurements using a flow cell, the setup (Supplementary Fig. S38c) was mounted on the beamline X-Y stage at a 45° angle to the incoming beam to maximize the fluorescence signal. All in-situ measurements were collected in fluorescence mode. Prior to measurement, the gas compartment (2-mm thick, 0.2 cm^3, cathodic chamber) was filled with He/N_2. Both the anolyte and catholyte were 1 M KOH. During CO$_2$RR, a 20 SCCM CO$_2$ gas flow was passed through the gas compartment. References data for oxide powders or metal foil were collected in transmission mode using ionization chambers, with the sampling chamber filled with N_2/He. For ex-situ samples, N_2/He was used to fill the cathodic chamber during XAS signal collection. ^{1}H NMR experiments were performed with a Bruker 400 MHz NMR spectrometer using a 5 mm broadband auto-tuneable probe with Z–gradients. Quantitative analysis of Cu loading in relevant samples was conducted via inductively coupled plasma mass spectrometry (ICP-MS, PerkinElmer, OPTIMA 7000DV). X-band EPR measurements (microwave frequency: 9.45597 GHz; power: 10 mW) were performed using an EPR MS-5000 spectrometer (Bruker, Germany). Samples were loosely packed into low-background 4 mm quartz paramagnetic tubes. Spectra were recorded with a modulation amplitude of 0.2 Gauss and a modulation frequency of 100 kHz. Raman measurements were conducted using a LABRAM HR EVO Raman microscope (equipped with a 50× objective, Leica, Germany) and a 532 nm laser. Acquisition parameters included an integration time of 6 s, 2 accumulations, a 600 nm grating, 10% laser power, and averaging over 3 scans per region.

CO$_2$ electrolysis measurement and product analysis

Electrochemical CO$_2$ reduction reaction (CO$_2$RR) experiments were performed in a thin liquid-electrolyte flow cell with a three-electrode configuration, controlled by a potentiostat (CHI1140C, data were exported as.txt files). The electrocatalyst (~4.0 mg) was mixed with 1 mL of 2-propanol and 10 µL of 5 wt% Nafion solution, followed by ultrasonication for 10 min to form an ink. The resulting ink (100 µL) was drop-cast onto a 28BC GDL (effective geometric area: 1 cm^2) and dried under an infrared lamp. The catalyst-coated 28BC GDL was used as the cathode, contacted with copper foil tape for conductivity. A Hg/HgO (1 M KOH) and a nickel plate (0.1-mm thick) served as the reference and counter electrodes, respectively. 1 M KOH electrolyte was pumped into the catholyte (~0.2 cm^3) and anolyte (~1 cm^3) compartments, separated by an anion exchange membrane (Fumasep FAB-PK-130). The electrolyte flow rates for the cathodic and anodic sides were 5–10 and 35–70 mL min^{-1}, respectively. The cathodic gas chamber (~0.15 cm^3) was continuously fed with 15–20 SCCM of CO$_2$ gas, controlled by a mass flow controller (CS200, Sevenstar). All applied potentials (unless stated otherwise) were calibrated to the reversible hydrogen electrode (RHE) with iR$_u$ drop compensation using the equation: $E_{RHE} = E_{Hg/HgO} + 0.14 + 0.0591$ pH $+ \eta_{IRu}$. R$_u$ was measured via electrochemical impedance spectroscopy (EIS) at open circuit potential (OCP). EIS parameters were set with an AC potential of 10 mV and frequency sweeps from 10^5 to 0.1 Hz. EIS data for Cu SACs were recorded in the same flow cell with a three-electrode configuration, using 1 M KOH as the supporting electrolyte. Impedance spectra were simulated using Zview.

For the calibration of the Hg/HgO electrode (1 M KOH), all electrochemical measurements were performed in a Teflon jar containing a redox solution to avoid any change in electrochemical activity caused by trace silicate contamination under ambient conditions. The redox solution was prepared by adding equimolar amounts of K$_4$[Fe(CN)$_6$] and K$_3$[Fe(CN)$_6$] to 1 M KOH (with a final concentration of ~1 mM for each). The Hg/HgO electrode and a Pt wire (serving as a counter electrode, though no current is required) were immersed in the redox solution. The OCP of the Pt wire versus the Hg/HgO electrode was measured using a potentiostat (CHI1140C). This OCP equals the formal potential of the redox couple (0.262 V) versus Hg/HgO. The measured OCP of the Hg/HgO electrode was verified to match this value (within ±5 mV) prior to use.

Gas product quantification was performed using an online gas chromatograph (Shimadzu, GC-2014C) equipped with a thermal conductivity detector (TCD) and a flame ionization detector (FID). Carrier gases included argon, nitrogen and hydrogen. Gas products were detected every 13 minutes using an automatic sampler to determine catalyst selectivity and corresponding partial current densities. The faradic efficiency (FE) of gas product was calculated using the following equation:

$$FE(\%) = \frac{nc\vartheta F}{IV} * 100\% \qquad (1)$$

where n is the number of electrons transferred, c is the product concentration (ppm) detected by gas chromatography, F is Faraday's constant, ϑ is the gas flow rate (SCCM) at the GC outlet, V is the molar volume (24.5 L mol^{-1} at 298.15 K), and I (mA) is the total current at the start of sampling.

Liquid products were quantified using an NMR spectrometer with water suppression and pre-saturation methods. NMR samples were prepared by mixing 0.5 mL of catholyte solution, 0.10 mL of D$_2$O, and 100 ppm (v/v) DMSO (added as an internal standard).

The electrochemical active surface area (ECSA) of the Cu SACs was calculated using the following equation: ECSA = R$_f$S, where S is the ideal areal capacitance (10 µF cm^{-2}) of a smooth carbon surface (in this work, S = 1 cm^2). The roughness factor (R$_f$) was estimated relative to the

ideal areal capacitance of a smooth carbon surface using the relation: Rf = C$_{dl}$/(10 µF cm^{-2}). The double-layer capacitance (C$_{dl}$) was determined by measuring the capacitive current associated with double-layer charging from the scan rate dependence of cyclic voltammograms (CVs) (Supplementary Fig. S35). Specifically, C$_{dl}$ was estimated by plotting j$_{capacity}$ = (j$_a$ − j$_c$)/2 at 1.058 V versus RHE against the scan rate, where the slope corresponds to C$_{dl}$. Here, j$_a$ and j$_c$ represent anodic and cathodic current densities, respectively.

In situ ATR-SEIRAS measurement

In situ ATR-SEIRAS tests were performed using a Fourier transform infrared (FTIR) spectrometer (Thermo Fisher Nicolet iS50) equipped with a Pike Technologies VeeMAX III ATR accessory and an MCT-A detector. A gold film was deposited on the Si prism via magnetron sputtering. The electrocatalyst (~3.2 mg) was mixed with 1 mL of 2-propanol and 20 µL of 5 wt% Nafion solution, followed by ultrasonication for 15 min to form an ink. The resulting ink was drop-cast onto the Au surface and dried under an infrared lamp. The Si prism was assembled into a home-made cell, with a graphite rod and an Ag/AgCl (saturated KCl) electrode serving as the counter and reference electrodes, respectively. During measurements, 0.5 M KHCO$_3$ electrolyte was pre-saturated and continuously bubbled with CO$_2$ gas. All spectra were recorded at designated potentials from 0 to −1.3 V vs. RHE, with a resolution of 4 cm^{-1} and 64 scans.

Calculations

All DFT calculations were performed using the projector-augmented wave (PAW) method as implemented in the Vienna ab initio simulation package (VASP 5.4.4)[49–52]. The revised Perdew–Burke–Ernzerh (PBE) functional (generalized gradient approximation) was used as the exchange-correlation functional, with long-range dispersion correction from Grimme's DFT-D3 method, and a kinetic energy cutoff of 450 eV was employed[53]. To describe localized Cu 3d electrons, the Hubbard model (DFT + U) was used with a U–J value of 3.0 eV[54]. The CuN$_4$ SAC was modelled in a supercell with a vacuum thickness >20 Å along the z-direction. The Brillouin zone was sampled using gamma-cantered 1 × 1 × 1 k-points generated via the Monkhorst-Pack scheme. Structural optimization was considered converged when the residual force on each ion was <0.01 eV Å^{-1} and the energy difference between consecutive iterations was <10^{-5} eV per atom.

On this basis, we simulated the adsorption behaviour of the *COOH, *CO, *CHO, *OCH$_2$, *OCH$_3$, *O and *OH intermediates for each catalyst, with each model optimized to convergence. The free energy change (ΔG) for each ECM step was calculated using the computational hydrogen electrode (CHE) model via the equation:

$$\Delta G = \Delta E + \Delta ZPE - T\Delta S + \Delta G_U + \Delta GpH \qquad (2)$$

where ΔE is the total energy change from DFT calculation, ΔZPE is the zero-point energy change, T is temperature (298.15 K), and ΔS is the entropy change. Entropy was calculated using a harmonic oscillator approximation. The effect of applied bias on the free energy of electron transfer steps was assessed using $\Delta G_U = -neU$ (where U is the electrode potential relative to RHE, e is the elementary charge, and n is the number of electrons transferred). ΔGpH = 0.0591*pH. For the CHE model, acidic (pH = 0) and alkaline (pH = 14) conditions yielded identical results. Explicit solvent model calculations were performed to evaluate solvent effects in 1 M KOH (containing 55 H$_2$O molecules and 1 KOH molecule). All DFT energies, zero-point energies, and temperature-entropy corrections (T*S, T = 298.15 K) for relevant species are provided in Supplementary Tables 9 and 10.

The DFT-based climbing-image nudged elastic band (CI-NEB) method was employed[55]. The initial structure was a Cu SA model with a 7-Cu-atom cluster, and the final structure was a defect model supporting an 8-Cu-atom cluster. After optimizing the initial and final

structures, six transition state points were inserted using the VTST tool, and CI-NEB calculations were performed with a force convergence criterion of 0.05 eV Å^{-1}.

Data availability

All data generated in this study are provided in the Supplementary Information/Source data file. Source data are provided with this paper.

References

1. Artz, J. et al. Sustainable conversion of carbon dioxide: an integrated review of catalysis and life cycle assessment. *Chem. Rev.* **118**, 434–504 (2018).
2. Li, F. et al. Molecular tuning of CO_2-to-ethylene conversion. *Nature* **577**, 509–513 (2020).
3. Fan, M. et al. Single-site decorated copper enables energy- and carbon-efficient CO_2 methanation in acidic conditions. *Nat. Commun.* **14**, 3314 (2023).
4. Li, L. et al. Hydrophobicity graded gas diffusion layer for stable electrochemical reduction of CO_2. *Angew. Chem. Int. Ed.* **61**, e202208534 (2022).
5. Qiao, J., Liu, Y., Hong, F. & Zhang, J. A review of catalysts for the electroreduction of carbon dioxide to produce low-carbon fuels. *Chem. Soc. Rev.* **43**, 631–675 (2014).
6. Nitopi, S. et al. Progress and perspectives of electrochemical CO_2 reduction on copper in aqueous electrolyte. *Chem. Rev.* **119**, 7610–7672 (2019).
7. Wu, H. et al. Selective and energy-efficient electrosynthesis of ethylene from CO_2 by tuning the valence of Cu catalysts through aryl diazonium functionalization. *Nat. Energy* **9**, 422–433 (2024).
8. Tan, X. et al. Stabilizing copper by a reconstruction-resistant atomic Cu–O–Si interface for electrochemical CO_2 reduction. *J. Am. Chem. Soc.* **145**, 8656–8664 (2023).
9. Li, L. et al. Hydrophobicity graded gas diffusion electrode with enhanced CO intermediate coverage for high-performance electroreduction of CO_2 to ethylene. *Appl. Catal. B Environ.* **331**, 122597 (2023).
10. Sun, L., Wang, Y., Guan, N. & Li, L. Methane activation and utilization: current status and future challenges. *Energy Technol.* **8**, 1900826 (2020).
11. Hori, Y., Wakebe, H., Tsukamoto, T. & Koga, O. Electrocatalytic process of CO selectivity in electrochemical reduction of CO_2 at metal electrodes in aqueous media. *Electrochim. Acta* **39**, 1833–1839 (1994).
12. Hori, Y., Kikuchi, K., Murata, A. & Suzuki, S. Production of methane and ethylene in electrochemical reduction of carbon dioxide at copper electrode in aqueous hydrogencarbonate solution. *Chem. Lett.* **15**, 897–898 (1986).
13. Ju, W. et al. Understanding activity and selectivity of metal-nitrogen-doped carbon catalysts for electrochemical reduction of CO_2. *Nat. Commun.* **8**, 944 (2017).
14. Rong, W. et al. Size-dependent activity and selectivity of atomic-level copper nanoclusters during CO/CO_2 Electroreduction. *Angew. Chem. Int. Ed.* **60**, 466–472 (2021).
15. Zhang, Y. et al. Coordination environment dependent selectivity of single-site-Cu enriched crystalline porous catalysts in CO_2 reduction to CH_4. *Nat. Commun.* **12**, 6390 (2021).
16. Zou, H. et al. Electronic perturbation of copper single-atom CO_2 reduction catalysts in a molecular way. *Angew. Chem. Int. Ed.* **62**, e202217220 (2023).
17. Osella, S. & Goddard, W. A. CO_2 Reduction to methane and ethylene on a single-atom catalyst: a grand canonical quantum mechanics study. *J. Am. Chem. Soc.* **145**, 21319–21329 (2023).
18. Shi, G. et al. Constructing Cu–C bonds in a graphdiyne-regulated Cu single-atom electrocatalyst for CO_2 reduction to CH_4. *Angew. Chem. Int. Ed.* **61**, e202203569 (2022).
19. Cai, Y. et al. Insights on forming N,O-coordinated Cu single-atom catalysts for electrochemical reduction CO_2 to methane. *Nat. Commun.* **12**, 586 (2021).
20. Dai, Y. et al. Manipulating local coordination of copper single atom catalyst enables efficient CO_2-to-CH_4 conversion. *Nat. Commun.* **14**, 3382 (2023).
21. Zhao, P. et al. Construction of low-coordination Cu–C2 single-atoms electrocatalyst facilitating the efficient electrochemical CO_2 reduction to methane. *Angew. Chem. Int. Ed.* **62**, e202314121 (2023).
22. Zhang, Z. et al. Distance effect of single atoms on stability of cobalt oxide catalysts for acidic oxygen evolution. *Nat. Commun.* **15**, 1767 (2024).
23. Jin, H. et al. Regulating the electronic structure through charge redistribution in dense single-atom catalysts for enhanced alkene epoxidation. *Nat. Commun.* **14**, 2494 (2023).
24. Wang, B. et al. A site distance effect induced by reactant molecule matchup in single-atom catalysts for fenton-like reactions. *Angew. Chem. Int. Ed.* **61**, e202207268 (2022).
25. Shan, J. et al. Metal-metal interactions in correlated single-atom catalysts. *Sci. Adv.* **8**, eabo0762 (2022).
26. Jin, Z. et al. Understanding the inter-site distance effect in single-atom catalysts for oxygen electroreduction. *Nat. Catal.* **4**, 615–622 (2021).
27. Lee, H. A., Park, E. & Lee, H. Polydopamine and its derivative surface chemistry in material science: a focused review for studies at KAIST. *Adv. Mater.* **32**, 1907505 (2020).
28. Salomäki, M. et al. Polydopamine nanoparticles prepared using redox-active transition metals. *J. Phys. Chem. B* **123**, 2513–2524 (2019).
29. Lee, H., Dellatore, S. M., Miller, W. M. & Messersmith, P. B. Mussel-inspired surface chemistry for multifunctional coatings. *Science* **318**, 426–430 (2007).
30. Ball, V. et al. Comparison of synthetic dopamine-eumelanin formed in the presence of oxygen and Cu^{2+} cations as oxidants. *Langmuir* **29**, 12754–12761 (2013).
31. Bernsmann, F. et al. Dopamine-melanin film deposition depends on the used oxidant and buffer solution. *Langmuir* **27**, 2819–2825 (2011).
32. Han, L. et al. A single-atom library for guided monometallic and concentration-complex multimetallic designs. *Nat. Mater.* **21**, 681–688 (2022).
33. Qu, Y. et al. Direct transformation of bulk copper into copper single sites via emitting and trapping of atoms. *Nat. Catal.* **1**, 781–786 (2018).
34. Sui, X. et al. Advanced support materials and interactions for atomically dispersed noble-metal catalysts: from support effects to design strategies. *Adv. Energy Mater.* **12**, 2102556 (2022).
35. Li, J. et al. Highly active and stable metal single-atom catalysts achieved by strong electronic metal-support interactions. *J. Am. Chem. Soc.* **141**, 14515–14519 (2019).
36. Arčon, I., Mirtič, B. & Kodre, A. Determination of valence states of chromium in calcium chromates by using X-ray Absorption Near-Edge Structure (XANES) spectroscopy. *J. Am. Ceram. Soc.* **81**, 222–224 (1998).
37. Li, Q. et al. Fe isolated single atoms on S, N codoped carbon by copolymer pyrolysis strategy for highly efficient oxygen reduction reaction. *Adv. Mater.* **30**, 1800588 (2018).
38. Kumar, A. et al. Moving beyond bimetallic-alloy to single-atom dimer atomic-interface for all-pH hydrogen evolution. *Nat. Commun.* **12**, 6766 (2021).
39. Yin, J. et al. Customizable CO_2 electroreduction to C1 or C2+ products through Cuy/CeO_2 interface engineering. *ACS Catal.* **12**, 1004–1011 (2022).
40. Zhao, J. et al. Modulation of *CH$_x$O adsorption to facilitate electrocatalytic reduction of CO_2 to CH_4 over Cu-based catalysts. *J. Am. Chem. Soc.* **145**, 6622–6627 (2023).
41. Li, Z. et al. Interface-enhanced catalytic selectivity on the C2 products of CO_2 electroreduction. *ACS Catal.* **11**, 2473–2482 (2021).

42. Chen, X. et al. Highly stable layered coordination polymer electrocatalyst toward efficient CO_2-to-CH_4 conversion. *Adv. Mater.* **36**, 2310273 (2024).

43. Handoko, A. D., Wei, F., Jenndy, Yeo, B. S. & Seh, Z. W. Understanding heterogeneous electrocatalytic carbon dioxide reduction through operando techniques. *Nat. Catal.* **1**, 922–934 (2018).

44. Su, J. et al. Strain enhances the activity of molecular electrocatalysts via carbon nanotube supports. *Nat. Catal.* **6**, 818–828 (2023).

45. Hammer, B. & Norskov, J. K. Why gold is the noblest of all the metals. *Nature* **376**, 238–240 (1995).

46. Nørskov, J. K., Abild-Pedersen, F., Studt, F. & Bligaard, T. Density functional theory in surface chemistry and catalysis. *PNAS* **108**, 937–943 (2011).

47. Wang, T. et al. Single-atom anchored curved carbon surface for efficient CO_2 electro-reduction with nearly 100% CO selectivity and industrially-relevant current density. *Adv. Mater.* **35**, e2205553 (2023).

48. Han, G. et al. Substrate strain tunes operando geometric distortion and oxygen reduction activity of CuN_2C_2 single-atom sites. *Nat. Commun.* **12**, 6335 (2021).

49. Kresse, G. & Hafner, J. Ab initio molecular dynamics for liquid metals. *Phys. Rev. B* **47**, 558–561 (1993).

50. Kresse, G. & Hafner, J. Ab initio molecular-dynamics simulation of the liquid-metalamorphous- semiconductor transition in germanium. *Phys. Rev. B* **49**, 14251–14269 (1994).

51. Blöchl, P. E. Projector augmented-wave method. *Phys. Rev. B* **50**, 17953–17979 (1994).

52. Joubert, D. From ultrasoft pseudopotentials to the projector augmented-wave method. *Phys. Rev. B Condens. Matter Mater. Phys.* **59**, 1758–1775 (1999).

53. Perdew, J. P., Burke, K. & Ernzerhof, M. Generalized gradient approximation made simple. *Phys. Rev. Lett.* **77**, 3865–3868 (1996).

54. Dudarev, S. L., Botton, G. A., Savrasov, S. Y., Humphreys, C. J. & Sutton, A. P. Electron-energy-loss spectra and the structural stability of nickel oxide: An LSDA + U study. *Phys. Rev. B* **57**, 1505–1509 (1998).

55. Sheppard, D., Terrell, R. & Henkelman, G. Optimization methods for finding minimum energy paths. *J. Chem. Phys.* **128**, 134106 (2008).

Acknowledgements

Author contributions

X.Z., Y.T. and H.C. supervised this project. L.L. carried out material synthesis, characterization, electrochemical experiments, and data analyses. X.L. implemented DFT calculations. Z.Z., H.C. (Haohui Chen), Y.D., and Y.Z. performed electrochemical measurements. J.C. performed characterization. L.L. drafted the manuscript with input from all other authors. All authors discussed the results and contributed to the final manuscript.

Competing interests

The authors declare no competing interests.

Additional information

Supplementary information The online version contains supplementary material available at https://doi.org/10.1038/s41467-025-63781-9.

Correspondence and requests for materials should be addressed to Yongbing Tang, Xiaolong Zhang or Hui-Ming Cheng.

Peer review information *Nature Communications* thanks the anonymous reviewers for their contribution to the peer review of this work. A peer review file is available.

Reprints and permissions information is available at http://www.nature.com/reprints

Publisher's note Springer Nature remains neutral with regard to jurisdictional claims in published maps and institutional affiliations.